The influence of microstructure on the sintering process in crystalline metal powders investigated by positron lifetime spectroscopy: I. Electrolytic and spherical copper powders



1999 J. Phys.: Condens. Matter 11 1757

(http://iopscience.iop.org/0953-8984/11/7/009)

J. Phys.: Condens. Matter **11** (1999) 1757–1786. Printed in the UK PII: S0953-8984(99)80630-4

# The influence of microstructure on the sintering process in crystalline metal powders investigated by positron lifetime spectroscopy: I. Electrolytic and spherical copper powders

T E M Staab†§, R Krause-Rehberg†, B Vetter‡ and B Kieback‡

† Martin-Luther Universität Halle-Wittenberg, Fachbereich Physik, Friedemann-Bach-Platz 6, D-06108 Halle/Saale, Germany

‡ Technische Universität Dresden, Institut für Werkstoffwissenschaften, Momsenstraße 13, D-01062 Dresden, Germany

Received 3 January 1997, in final form 4 November 1998

**Abstract.** We investigate the influence of microstructure (dislocations, and grain and subgrain boundaries) on the sintering process in compacts of electrolytic and spherical copper powders by means of positron lifetime spectroscopy. We compare the lifetime data obtained to the kinetics of the annealing out of vacancy clusters after low-temperature electron irradiation, and the kinetics of recovery and recrystallization after plastic deformation. The change of powder-particle and grain sizes with temperature is determined in a complementary study by metallography and x-ray line-profile analysis. At the intensive-shrinkage stage, the effective powder-particle size in electrolytic copper powder is $\approx 5\ \mu$m and the grain size is $\approx 2\ \mu$m. Due to the dendritic morphology of the powder, the effective powder-particle size is much smaller than that determined by particle-size analysis ($\approx 34\ \mu$m). Because of the small powder-particle and grain sizes, a measurable fraction of positrons annihilate at grain boundaries and in surface states, i.e. at inner pore surfaces. At higher temperatures ($T > 550\ ^\circ$C), grain boundaries are, besides a small surface component for compacts of electrolytic powder, the only detectable lattice defects in both powders. We find that the observed shrinkage rates can be explained—at least qualitatively—by *Coble* creep, while *Nabarro–Herring* and *Kosevic* (dislocation) creep seem to play only a minor role in the systems investigated.

## 1. Introduction

Sinter metals are used in many technical applications. But the theoretical foundations for describing the sintering process in compacts of crystalline metal powder used in technical applications—especially the high shrinkage rates—have up to now remained controversial. If we speak of sintering in the following, we always mean *pressureless* sintering, i.e. sintering without any external pressure applied during heating. The first processing step is to give the powder compact the desired shape by compacting—e.g. by uniaxially pressing—a powder (metal or ceramic) to a certain green density (the green density is the fraction of the maximum theoretical density—that of the solid of same material). Typical values vary between 0.6 and 0.8. By *contact boundary* we mean the contact between two powder particles which develops during heating from the pure pressing contact. The contact boundaries are changed during further heating to large-angle grain boundaries. *Sintering* means heating a compact up to about $4/5$ of its melting temperature and holding it at this temperature for a certain time. The

§ Present address: Helsinki University of Technology, Laboratory of Physics, PO Box 1100, FIN-02015 HUT, Finland.

0953-8984/99/071757+30$19.50  

observed shrinkage is a pressureless process caused by the minimizing of the free energy due to the reduction of the internal and external surfaces. This driving force has been known for a long time. While the mechanisms for achieving this are known for model systems [1–3], they are still under discussion for defect-rich real powder compacts, i.e. samples produced from powders used in technical applications, for which defect-induced diffusion was proposed to explain the observed high shrinkage rates [4–7].

The observed shrinkage depends on the morphology of the powder, i.e. the powder-particle size and shape, grain and subgrain sizes, and dislocation density (intrinsic parameters), and also on extrinsic parameters such as the pressure, heating rate, sintering temperature, and atmosphere. There are three shrinkage stages. In the initial stage the sharp curvature gradients, resulting from the pressing, are reduced—often via surface diffusion (this does not lead to shrinkage). In the intermediate stage the pores have become rounded, and are often nearly cylindrical and fully interconnected. The final stage is characterized by closed, spherical pores. Note that there is no clear distinction between the stages.

Apparently, the diffusion is realized by a vacancy mechanism, since the vapour pressure is, up to the melting temperature, sufficiently low to exclude the possibility of material transport by evaporation/condensation for the metals investigated [8]. Due to the limited range of the Laplace tension, powder particles must contain defects which will act as sources and sinks for vacancies in comparatively high densities. Considering, e.g., grain boundaries, the grain size has to be at least an order of magnitude smaller than the powder-particle size. But what are the vacancy sources and sinks? There are different models describing sintering as a high-temperature creep process in crystalline materials. The powder-particle size has the major influence on the driving force (which is proportional to the inverse particle size), while large-angle grain boundaries (*diffusional* or *Nabarro–Herring creep*: $\propto$ inverse grain size squared) as well as dislocations (*dislocation* or *Kosevic creep*: $\propto$ dislocation density) are assumed to play an important role as vacancy sources and sinks. In the case of *Coble creep* ($\propto$ inverse grain size cubed), vacancy transport is itself assumed to happen in grain boundaries (grain boundary diffusion).

In this paper we do not aim to give a precise quantitative picture of different sintering mechanisms. The samples investigated here were mostly produced from powders used in technical applications, which are not well suited for use as model systems. But we do try to make a qualitative distinction between different models proposed previously.

We investigate sintering by following the shrinkage and shrinkage rate *in situ* using a high-temperature dilatometer. To work out which shrinkage mechanism is dominant, we try to monitor the defects on an atomic scale. For the defect investigations, we interrupt the sintering process by quickly cooling the samples sintered to a certain stage. By means of positron lifetime spectroscopy (POLIS) together with metallographic studies, x-ray line-profile analysis, and transmission electron microscopy (TEM), we try to obtain information about the parameters influencing the sintering process via different mechanisms, i.e. the dislocation density, the grain sizes, and the density of vacancy clusters if present. Unfortunately, it is not possible to make measurements with the samples *in situ* (see the discussion in [9]).

Positron lifetime spectroscopy has become established in the last 20 years as a powerful tool for detecting lattice defects on an atomic scale in metals and semiconductors. Possible positron traps in metals include: dislocations, monovacancies, vacancy clusters (sometimes called microvoids—consisting of up to some ten vacancies), small and large-angle grain boundaries, as well as internal surfaces (voids or pores). These defects can be detected separately (as can their respective densities) using lifetime spectroscopy. But it is the densities of these defects that are the decisive parameters in the sintering models described above. Nevertheless, we have to keep in mind that there are similar signals from different kinds of

lattice defect, and hence some defects are not distinguishable *ab initio* [9]. Examples include dislocations/monovacancies (typically with lifetimes of 170 ps) and grain boundaries/vacancy clusters (typically with lifetimes of 300 ps), respectively. For metallic surfaces or large voids ($>50$ vacancies), a positron lifetime of about 500–600 ps is found (for a review, see [10], [11], or [9]). Furthermore, POLIS and x-ray diffraction studies are integral methods. This means that one has to assume a specific defect model when analysing the data, e.g. even or discontinuously distributed defects (see [9] for a review).

If defects are present in the sample, the positrons can be trapped prior to annihilation. The probability for this, i.e. the trapping rate, is proportional to the defect density [12,13]. The lower electron density in defects with open volumes, such as dislocations, vacancies, and vacancy clusters, results in a longer lifetime for the trapped positron. The lifetime spectra are analysed in terms of two or more components, i.e. as a sum of exponentials after source/background subtraction and deconvolution of the experimental resolution function. This gives the positron lifetimes and intensities [14, 15]. By *bulk lifetime* ($\tau_b$) we mean the average positron lifetime in an undisturbed crystal, while $\tau_1$ always means a *reduced bulk lifetime* where the reduction is due to the presence of defects. By *vacancy lifetime*, *cluster lifetime*, etc, we do not mean the lifetime of this kind of defect, but the lifetime of a positron in the vacancies, vacancy clusters, etc. For a detailed review, see [9]. If we are monitoring grain boundaries with positrons, then the defects are not continuously distributed, i.e. the standard trapping model does not apply. If we detect a grain boundary signal, then all of the volume inside the grains is scanned by positrons, since otherwise the positrons would not be able to reach the grain boundary. The same is true for powder-particle surfaces.

Using different powder-particle sizes, different fractions of the total signal stem from the contact boundaries (pressing contact) and surrounding areas, due to the limited positron diffusion length [16]. Hence, it is necessary to determine grain sizes inside powder particles by metallographic methods—as well as the powder-particle sizes and their size distribution.

As complementary investigations, we carried out the annealing out of radiation-generated defects, i.e. vacancies and (during annealing) vacancy clusters, and the annealing out of defects generated by plastic deformation, i.e. monitoring recovery and recrystallization. Even though the results are known from the literature, we performed these measurements to obtain up-to-date accurate positron lifetime values for dislocations and monovacancies, and typical ones for vacancy clusters (see also [9] and [17] for more details). Furthermore, the aim of these investigations was to compare what is happening owing to pressing the powders and subsequently sintering the samples, and to establish which defects may be generated, and when they anneal. Another aim was to carry out the deformation/irradiation and subsequent annealing of the sintered state—in this way excluding any influences of impurities in the sinter powders, while the investigations on pure compact material were only for comparison and to check the measured lifetimes of positrons in defects.

Using these facts and results on the kinetics of the annealing out of defects, recovery, and grain growth, one can judge which kind of defect may be detected at certain temperatures. Finally, we try to point out what consequences the detected defect characteristic has for the different shrinkage mechanisms.

We investigate compacts of copper powder as an example representing the fcc metals in part I. We will consider compacts of tungsten powders with different particle sizes as examples representing the bcc metals in part II. Part III will be concerned with compacts of nickel reduction powder.

The outline of this article is as follows. The experimental set-up and the treatment of different samples are described in section 2. Section 3 contains the experimental results on the behaviour of defects during sintering and the complementary measurements. In section 4 we

discuss the results for sintering in the light of the results from the complementary investigations, and give the relevant equations for describing the sintering process as high-temperature creep. Finally, section 5 contains our conclusions.

## 2. Experiments

In this section we explain the special features of the sintering powders under investigation, the experimental set-up, and how we treated the samples during the different measurements.

### *2.1. Electrolytic copper powder*

We used electrolytic copper powder, supplied by Norddeutsche Affinerie Hamburg, with an average particle size determined by particle-size analysis to be 34 $\mu$m (see table 1), a purity of 99.75%, and an oxygen content of 0.12%. This powder has a very complicated morphology. Dendritic particle shapes lead to an effective powder-particle size after pressing which is different from the particle size measured by, e.g., screening analysis. This is because the dendritic arms break during the pressing of the compact, leading to lots of very small copper particles and sometimes to wide areas of compact copper, and hence to a very inhomogeneous 'powder-particle size distribution' in the compact. Hence, it is hardly appropriate to speak of separate particles at all. Furthermore, even the uncompacted powder seems to have a complicated microstructure inside each powder particle, i.e. there are large- and small-angle grain boundaries, and possibly dislocations. This can be due to the production process, in which copper is precipitated in an aqueous solution of copper sulphate at about 50–60 °C. This means that copper crystals grow irregularly at the cathode, and hence grain boundaries as well as dislocations become plausible. Usually, the process of pressing is thought to create new defects as a result of plastic deformation of individual powder particles. It is obvious that dislocations are not generated if the grain size is very small, i.e. below 1 $\mu$m, since the Frank–Read source mechanism simply cannot operate then.

**Table 1.** The particle size distributions for electrolytic and spherical copper powder. The analysis was performed in the case of the electrolytic powder using a laser granulator, 'Analysette 22' (Fritsch GmbH, Idar-Oberstein, Germany).

| Powder | d10 ($\mu$m) | d50 ($\mu$m) | d90 ($\mu$m) |
|---|---|---|---|
| Electrolytic copper | 14.1 | 34.1 | 62.3 |
| Spherical copper | 10.7 | 19.6 | 34.0 |

### *2.2. Spherical copper powder*

As a second example, we considered spherical copper powder of 99.7% purity supplied by ALCAN Powders & Pigments, New Jersey (USA). This powder is produced by gas evaporation. The powder showed a hydrogen loss of 0.16 wt%. The average particle size is about 19 $\mu$m, and the particles have nearly spherical shapes. See table 1.

### *2.3. Sintering*

The different samples were pressed under a uniaxial pressure of 300 MPa and then sintered at the TU Dresden, where the measurements required for plotting the shrinkage curves were made *in situ* by a high-temperature dilatometer, i.e. we were continuously monitoring the shrinkage

(corrected for thermal expansion) as a function of temperature and time. We generally used a reducing hydrogen atmosphere, with one exception where argon was used (the heating rate was 10 K $min^{-1}$ for the compacts of electrolytic copper powder). The sintering temperature of 900 °C corresponds to a homologous temperature of $T_S = 0.87\ T_M$, where $T_M$ is the melting temperature of copper in degrees Kelvin. Samples for investigation by POLIS were prepared by sintering small discs in the furnace up to the appropriate temperature at the corresponding heating rate, and then cooling them to room temperature by quickly removing them from the furnace and hence 'freezing' a certain stage of the sintering process. This is justified because most of the processes involve an exponential dependence on temperature.

### *2.4. Positron lifetime measurement*

For the positron lifetime spectroscopy, two identical samples (discs of 11.5 mm diameter and approximately 1 mm thickness) were prepared for each temperature or time. These samples were used later for x-ray diffraction and metallographic studies, and were prepared for TEM investigations. The samples were sintered as described above.

As a source for positrons, $^{22}$Na is often used. The positron source is a radioactive salt covered by a thin (2 $\mu$m) Al foil. As regards the spectra for the source annihilation part, see the discussion in [18]. For the measurements, the $^{22}$Na source is placed between two identical samples (a source–sample sandwich). To make measurements on uncompacted powder, some powder was poured into a small box. The positron source was then placed on top of the powder, and more powder was added on top until the box was full.

The spectrometer had a Gaussian-shaped time resolution of about 250 ps FWHM in a fast–fast coincidence set-up using plastic scintillators.

### *2.5. Electron irradiation and plastic deformation*

For the low-temperature (4 K) electron irradiation, sintered samples were prepared as described in [9]. All defects are annealed out prior to irradiation to below their detection limits; this is checked by making sure that the lifetime measurement always gives a single-component spectrum with the bulk lifetime of 112 ps. Then these samples were irradiated with 2 MeV electrons at 4 K. The measurement started at 90 K. The dominating defect type generated by the irradiation is assumed to be monovacancies, due to the electron energy being 2 MeV (for more details, see [9] or [17]). Dislocations are not likely to be present in these samples directly after irradiation.

For the deformation studies, sintered samples (900 °C, 12 h; i.e. samples heat treated such that no more shrinkage was observed) were pressed to different thickness reductions (for details, see [9] or [17]). The same sample pair was then successively annealed under vacuum at each temperature for 30 minutes, and then cooled to room temperature again before performing the lifetime measurement.

## 3. Results

In this section we will present the results obtained by the different methods used to characterize the microstructures of the samples. It is necessary to use other methods together with positron lifetime spectroscopy since, as mentioned in section 1, there are ambiguities in the interpretation of lifetime data if the powder-particle or grain sizes are smaller than about 15 $\mu$m, with the result that a measurable fraction of positrons—certainly depending on the defect densities

inside each particle or grain—are likely to reach the particle surface or grain boundary and become trapped there [16].

### *3.1. Metallography*

The samples investigated first by means of lifetime spectroscopy were embedded, then ground and polished, and finally we performed a grain boundary etching ('Hoffmanns Ätzmittel') to determine the grain sizes inside the powder particles.

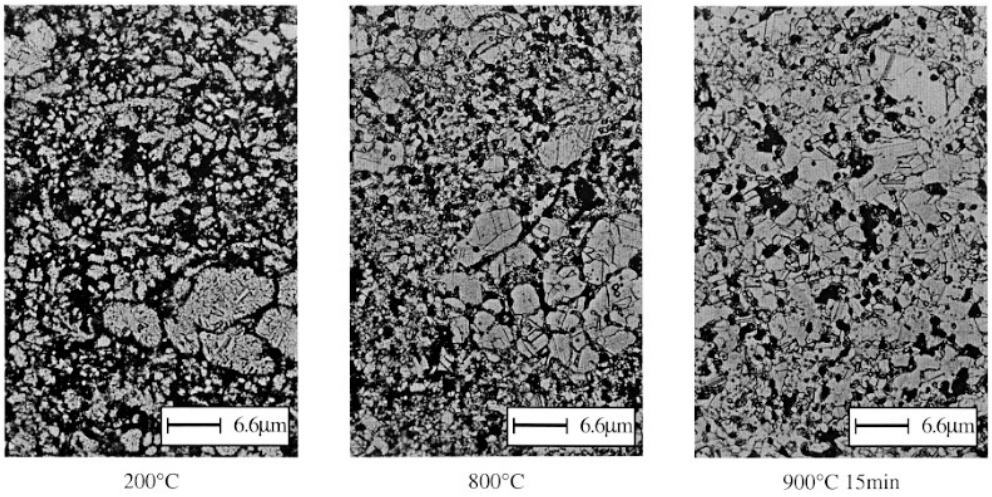


**Figure 1.** The development of the microstructure during sintering for compacts of electrolytic copper powder pressed to a green density of $\rho_g = 0.78\ \rho_0$ and heated at a rate of 50 K min$^{-1}$ up to 900 °C. Different stages of the sintering process are shown in the pictures as indicated by the temperatures given below them. Note the complicated microstructure inside the powder particles below $T = T_R = 0.4\ T_M$.

The first series of pictures (figure 1) shows the development of the microstructure for samples of electrolytic copper powder pressed to a green density of approximately $0.78\ \rho_0$ and then sintered to the appropriate temperature at a heating rate of 50 K min$^{-1}$. The second series (figure 2) shows compacts of spherical copper powder (heating rate: 10 K min$^{-1}$; $\rho_g \approx 0.75\ \rho_0$) treated in the same way. This powder is a better model substance, due to the nearly spherical powder-particle shapes. Hence, we see clearly visible pressing contacts becoming contact boundaries during the heat treatment.

*3.1.1. Electrolytic copper powder.* It turned out that in the uncompacted electrolytic powder the average grain size is less than 1 $\mu$m, which will be important in explaining the positron results. This result is supported by TEM investigations on these samples (see section 3.3).

The dendritic structure is apparently destroyed by pressing, and smaller pieces of the original powder particles now give an effective particle size much smaller than that measured by particle-size analysis of the original powder.

A series of photographs show the different stages of sintering: recrystallization twins appear for temperatures higher than 300 °C—indicating the onset of recrystallization, which is nearly complete at 400 °C. At higher temperature, i.e. for $T > 600$ °C, grain growth starts, and at 800 °C the pores begin to vanish.

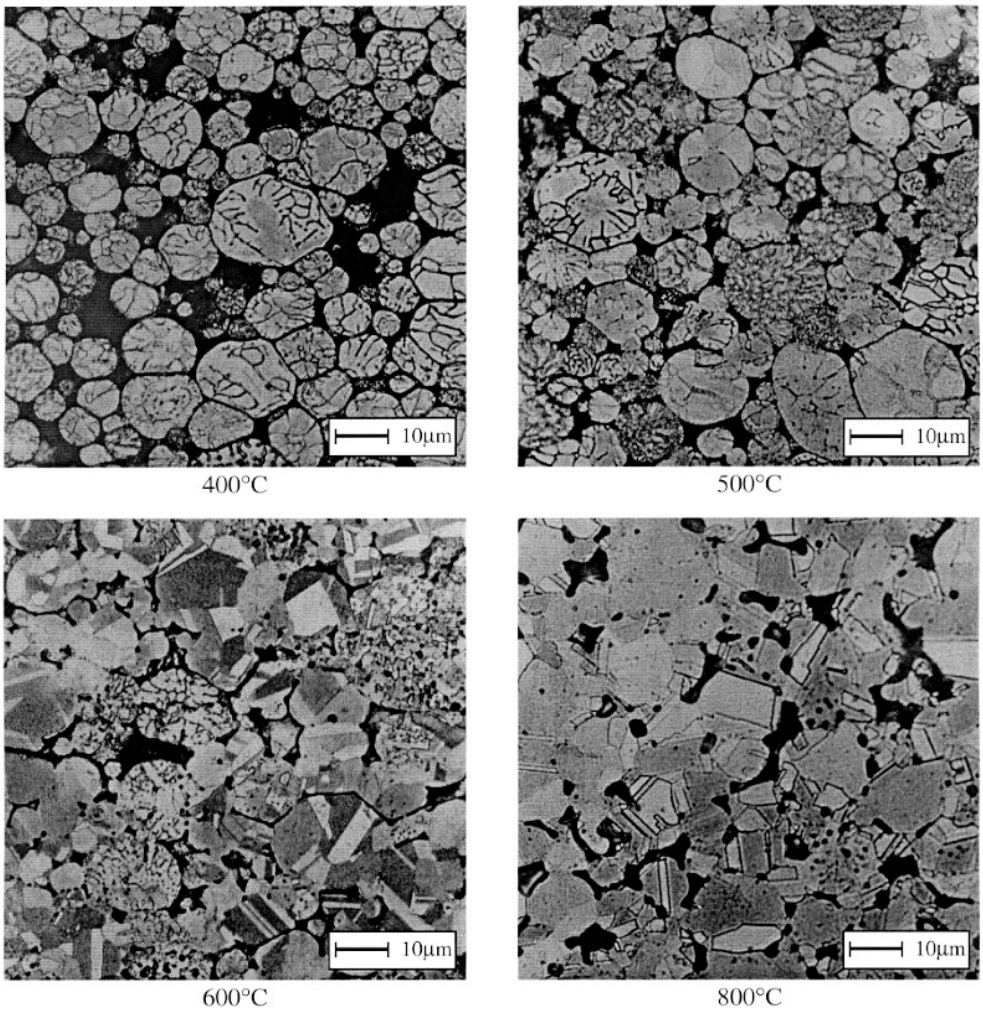


**Figure 2.** Compacts of spherical copper powder ($\bar{L}_P = 19\ \mu$m) pressed to a green density of $\rho_g = 0.75\ \rho_0$ and heated at a rate of 10 K min$^{-1}$ up to 900 °C; the pictures show the development of the microstructure during sintering, i.e. different stages of the sintering process as indicated by the temperatures given below the panels. Note the microstructural changes from 500 to 600 °C. The sintering process appears to start in the more sponge-like powder particles with smaller grain size.

*3.1.2. Spherical copper powder.* In the case of spherical copper powder, we found two different types of powder particle—one seems to be more solid, with an average grain size, after pressing and heating up to 400 °C, of about 5.8 $\mu$m, and the other is somewhat sponge-like, with an average grain size of 2.5 $\mu$m. Considerable grain growth starts at 500 °C, where we observe neck formation due to diffusion processes which begin to change the pure pressing contact, i.e. the edges of the contact area become rounded. At 600 °C the microstructure of the compact has changed completely, i.e. recrystallization twins have appeared and for some parts of the compact it is hardly appropriate to speak of individual particles. Furthermore, the grain size has increased nearly by a factor of 2 as determined by linear analysis and a

factor of 4 as determined from POLIS, i.e. from the lifetime data we estimate the fraction of positrons reaching grain boundaries by assuming that the defect-related lifetime component at about 280 ps occurs exclusively as a result of annihilation at the boundaries. This leads, by comparison to the Monte Carlo (MC) results, to an average grain size [9, 16]. The grain growth indicated accompanies a complete change of the microstructure in the powder compacts, while shrinkage is starting. It is apparent from the pictures that a complete change in the microstructure starts at the powder particles with a smaller average grain size.

### *3.2. Positron lifetimes—modelling positron diffusion*

We start with the assumption that positrons in powders or porous materials can thermalize† only within a powder particle or compact parts [9].

Hence positrons are assumed to stop inside compact material (thermalization) and then start diffusing (random-walk motion). For three-dimensional random-walk motion, the average diffusion length in defect-free copper is, according to [29]

$$L_+ = \sqrt{2d D_+ \tau_{\mathrm{eff}}}$$

about 330 nm, taking $D_+ = 1.6$ cm$^2$ s$^{-1}$ (the most recently obtained experimental value is $D_+ = 1.7 \pm 0.5$ cm$^2$ s$^{-1}$ [30], while theory gives $D_+ = 1.56$ cm$^2$ s$^{-1}$ [10]). During diffusion, it is possible for the positrons to reach inner surfaces—depending on the grain and powder-particle sizes, and on the density of positron traps inside the powder particles. If trapping sites are present, they change the annihilation parameters significantly. In the case in which we detect a surface component, a measurable part of the annihilation signal certainly stems from the contact boundaries and surrounding area.

A Monte Carlo (MC) simulation of the positron diffusion in porous or fine-grained materials showed that for copper, and for a powder-particle or grain size smaller than about 15 $\mu$m, a measurable fraction of positrons are able to reach the surfaces or interfaces, and so can become trapped there [16]. The expected positron lifetime in surface states can be estimated to be about 550 ps (see the discussion in [9, 17]).

The basic assumptions concerning the grain and powder-particle sizes are, roughly speaking, the following (for more details see [9]):

- Due to very large defect densities in the interfaces (large-angle grain boundaries), one can certainly assume that all positrons which reach that interface on their diffusion path (the disturbed region of the crystal) will become trapped there. Perhaps this is a type of precursor trap, and the positron will then diffuse along the interface to the larger open-volume traps detected, which are, perhaps, at the edges of grains.
- Positrons that reach the surfaces of powder particles on their diffusion path will certainly become trapped in a surface state, since the work function is negative for positrons for all of the metals investigated, and hence they will gain energy by passing through the surface [11]. The potential for positrons is attractive along the entire surface.
- If inside powder particles or grains there are positron traps other than the respective interfaces, they will be considered according to their corresponding trapping rates $\kappa$ (see the discussion in [16]).
- Spherical grain or powder-particle shapes were used, as they provide the simplest and most easily calculable model. Disregarding twin boundaries, which cannot trap positrons, one can see from the microscopic pictures that this gives fairly good results. Experience shows that approximations like this work astonishingly well.

† Thermalization results in the positron losing its initially high energy of up to 540 keV (see [9–11]).

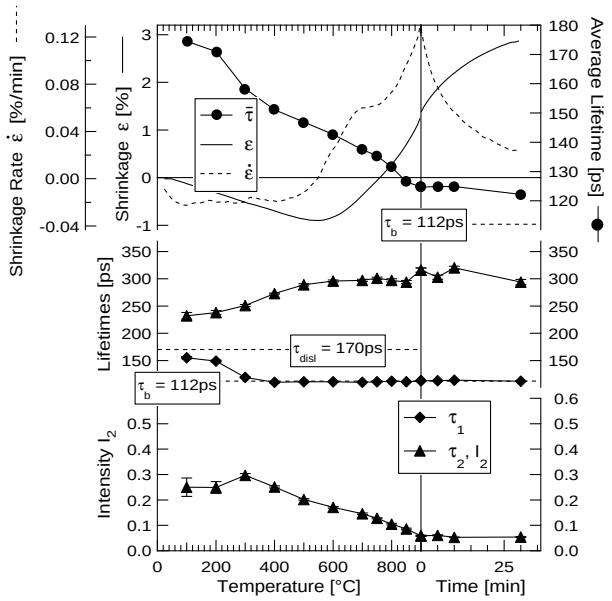


(a)

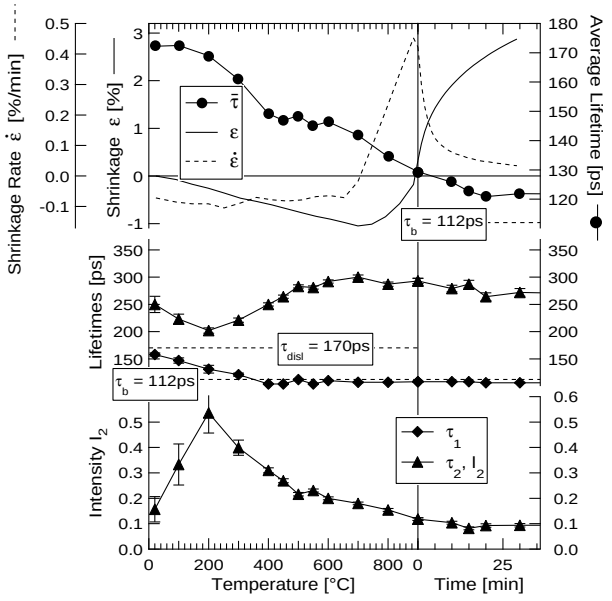


(b)

**Figure 3.** Compacts of electrolytic copper powder pressed (300 MPa) to a green density of $\rho_g = 0.78\ \rho_0$ and sintered at heating rates of 10 K min$^{-1}$ ($6.0 \times 10^6$ counts per spectrum) (a) and 50 K min$^{-1}$ ($1.5 \times 10^6$ counts per spectrum) (b); shown are the shrinkages and the shrinkage rates together with the average lifetimes (upper parts); in the lower parts, decompositions of the lifetime spectra are given.

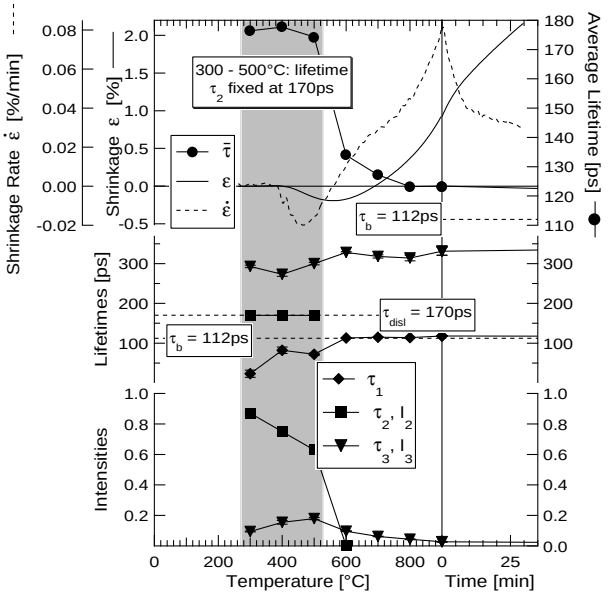


**Figure 4.** Spherical copper pressed ($\rho_g = 0.75\ \rho_0$) and sintered at 10 K min$^{-1}$ under $H_2$; the figure shows the shrinkage and the shrinkage rate together with the average lifetime (upper part), and a decomposition of the lifetime spectra (lower part). From 300 to 500 °C, $\tau_2$ was fixed at the dislocation value ($\tau_2 = \tau_{disl} = 170$ ps). The free decomposition at 500 °C gave $\tau_2 = 176 \pm 8$ ps.

Throughout this article, the analysis of positron data relating to porous or fine-grained samples (e.g. those given in figures 3 and 4) will be based on the first two natural assumptions. As regards the determination of grain and powder-particle sizes, we have to consider this together with the last two assumptions.

**Table 2.** Compacts of electrolytic copper powder (heating rate: 50 K min$^{-1}$): the average grain sizes from linear analysis (assuming nearly spherical grains) and estimated from POLIS data (using MC simulation results) for samples prepared at different temperatures. By 'fraction of $e^+$ at GB' we mean the fraction of the total number of positron annihilation events occurring at the grain boundaries (see the discussion in the text).

| | Metallography | POLIS | | |
|---|---|---|---|---|
| $T$ (°C) | Average grain size, $\bar{L}_G$ ($\mu$m) | $\tau_{GB}$ (ps) | Fraction of $e^+$ at GB | $\bar{L}^{MC}_{grain}$ ($\mu$m) |
| 20 | $\leqslant 2.4$ | $267 \pm 7$ | | $\leqslant 1.5$ |
| 400 | | $250 \pm 3$ | $33.0 \pm 3.5$ | $\leqslant 2.0$ |
| 600 | $\leqslant 2.4$ | $292 \pm 3$ | $18.2 \pm 3.0$ | $\approx 2.2$ |
| 800 | | $287 \pm 4$ | $12.5 \pm 2.5$ | $\approx 3$ |
| 900 | $3.1 \pm 1.0$ | $293 \pm 5$ | $9.0 \pm 2.0$ | $\approx 4$ |
| 900 (15 min) | $5.4 \pm 1.5$ | $287 \pm 7$ | $5.8 \pm 1.5$ | $\approx 6$ |

The results given in tables 2 and 3 are obtained as follows. First, we determine the fraction of positrons annihilating in dislocations and at grain boundaries from the primary positron data (lifetimes and intensities) by using the appropriate equations (see section 2

**Table 3.** Compacts of spherical copper powder: average grain sizes estimated from positron annihilation data (with the use of Monte Carlo simulation results) and from linear analysis (assuming nearly spherical grains) for samples prepared at different temperatures (see the discussion in the text).

| | Metallography | POLIS | | |
|---|---|---|---|---|
| $T$ (°C) | Average grain size, $\bar{L}_G$ ($\mu$m) | $\tau_{GB}$ (ps) | Fraction of $e^+$ at GB | $\bar{L}^{MC}_{grain}$ ($\mu$m) |
| 300 | $4.9 \pm 1.0$ | $293 \pm 5$ | $11.1 \pm 1.5$ | $\approx 1.0$ |
| 400 | $3.9 \pm 1.0$ | $273 \pm 5$ | $14.2 \pm 2.0$ | $\approx 1.0$ |
| 500 | $5.1 \pm 1.0$ | $300 \pm 3$ | $15.4 \pm 2.0$ | $\approx 1.0$ |
| 600 | $8.0 \pm 1.5$ | $328 \pm 3$ | $7.5 \pm 1.5$ | $4 \pm 1.0$ |
| 700 | $9.3 \pm 1.7$ | $318 \pm 4$ | $4.5 \pm 1.0$ | $6 \pm 1.5$ |
| 800 | $10.1 \pm 2.0$ | $314 \pm 7$ | $3.1 \pm 0.8$ | $9 \pm 2.0$ |
| 900 | $9.8 \pm 2.0$ | $331 \pm 10$ | $1.9 \pm 0.7$ | $10 \pm 2.0$ |
| 900 (2 h) | $12.2 \pm 3.0$ | $342 \pm 12$ | $1.1 \pm 0.5$ | $\geqslant 12$ |

of [9]) to obtain the fraction of positrons reaching the interfaces and surfaces. Second, we correlate this with the results of the Monte Carlo simulation of the positron diffusion [16]. This leads to rough estimates of powder-particle and grain sizes, assuming that the POLIS signal $\tau_{GB}$ with a lifetime of about 300 ps stems from grain boundaries exclusively. This is justified at least for temperatures higher than 500 °C, since, as we will see in sections 3.2.2 and 3.2.3, dislocations and vacancy clusters are not likely to exist at such high temperatures. Below 200 °C, the grain sizes estimated from the positron results could be too small. Analysis of the POLIS spectra reveals that there should be defect-free areas in the powder particles, since the decomposition gives, besides the signals for dislocations and vacancy-cluster/grain boundaries, the bulk lifetime. Perhaps there is no homogeneous distribution of dislocations in subgrains, i.e. dislocations are incorporated into subgrain walls. Another possibility is the existence of defect-free grains in addition to grains containing dislocations.

Complementary investigations of the annealing out of defects generated in pure copper and sintered samples annealed prior to deformation or irradiation will be presented, together with other complementary investigations on the annealing out of defects in uncompressed powder and the change of the defect structure that occurs during pressing.

*3.2.1. Sintering.* Some important observations on the analysis of the positron lifetime spectra in sintered samples are:

(a) At least three different types of defect are detectable by means of positrons.
(b) Even for the uncompressed powder, we measure a dislocation signal (lifetime: ≈160 ps; dislocations or small-angle grain boundaries), a vacancy-cluster-like signal (lifetime: 250–300 ps; vacancy clusters in the volume or large-angle grain boundaries), and a positron lifetime at surfaces (about 550 ps).

Due to the deformation caused by the pressing, dislocation glide and dislocation intersection should occur in the samples, and hence monovacancies should be generated due to jog dragging; these could form vacancy clusters since they are mobile at room temperature (see chapter 7.3 of [31]). This has to be seen in comparison to the generation of monovacancies after electron irradiation and subsequent annealing.

(i) *Electrolytic copper powder.* We sintered compacts of electrolytic copper powder at two different heating rates, i.e. 10 and 50 K $min^{-1}$ (see figure 3).

From the shrinkage rate, one sees a second maximum for a heating rate of 10 K $min^{-1}$—perhaps due to a different mechanism which acts at a lower temperature but cannot develop its effects during the more rapid heating. From 400 °C, the positron lifetime signal has only two main components: one which is nearly the bulk lifetime signal and another which looks like a signal for a positron lifetime in vacancy clusters, i.e. about 300 ps.

(ii) *Spherical copper powder.* We sintered compacts of this powder at only one heating rate (10 K $min^{-1}$). It shows a different annealing behaviour in comparison to the case for compacts of the electrolytic powder (see figure 4).

There is a very sharp decrease in the average lifetime between 500 and 600 °C, while for compacts of electrolytic powder the average lifetime decreases slowly over the whole temperature range. The apparent positron lifetime in dislocations of about 170 ps persists for much longer in the spectrum, i.e. up to 500 °C. The drastic fall of $\bar{\tau}$ from 500 to 600 °C is accompanied by a significant change in the microstructure of the samples (see the corresponding metallographic pictures in figure 2) and by the vanishing of the dislocation lifetime component (≈170 ps). The dislocation density drops from above $10^{11}$ $cm^{-2}$ to below $3 \times 10^8$ $cm^{-2}$. For temperatures higher than 600 °C, only two separate lifetime components are detected: $\tau_1 \approx \tau_b$ and $\tau_2 \approx \tau_{cl}$ (we did not detect a surface component for this compact). This is again inconsistent with the trapping model if we assume evenly distributed defects. In the temperature range above 600 °C, increasing shrinkage occurs with decreasing $I_2$.

*3.2.2. Electron irradiation.* One aim in investigating sintered samples together with high-purity bulk material was to work out whether the impurities in sinter material have any influence. For the sample material considered, no effect was found. See figure 5 and [17].

At low temperatures, i.e. from 90–215 K, the electron-irradiated samples show in the case of pure (4N7) copper a single one-component spectrum (with a $170 \pm 0.5$ ps lifetime). We can attribute this lifetime to monovacancies in the copper samples, since at the electron energies of 2 MeV that were used only monovacancies are likely to be generated. For the well annealed sintered samples, there is a two-component spectrum after irradiation. The second lifetime of about $170 \pm 1$ ps can certainly be attributed to monovacancies as well.

At temperatures slightly higher than $T = 220$ K, monovacancies in pure copper are, due to the vacancy migration enthalpy of about $0.76 \pm 0.04$ eV, known to become mobile (see [19, 32]). Mobile monovacancies apparently form vacancy clusters, as indicated by a second defect-related lifetime of about $\bar{\tau}_3 = 255 \pm 10$ ps (the average from a free three-component decomposition over the temperature range 251–370 K). This positron lifetime indicates a cluster size of 4–5 vacancies (for further details, see [17] and [9]).

The vacancy-cluster signal vanishes at about 393 K (120 °C), hence indicating that the vacancy-cluster density drops below $4 \times 10^{-8}$ per atom and that this defect is no longer detectable using positrons. For more details, see [9].

*3.2.3. Plastic deformation.* As a second example, we considered defects generated by plastic deformation (pressing) of samples that had been sintered for several hours at the sintering temperature (900 °C) so that no changes in the shrinkage were observed any longer; see section 3.2.1. We present here only the main results. For details, see [9]. See also figure 6.

Measurements were made on all samples prior to deformation. While pure copper bulk samples showed a single-lifetime spectrum (bulk lifetime: 112 ps), the sintered samples showed a spectrum reflecting mainly the bulk lifetime but also a defect-related lifetime of about 250 ps

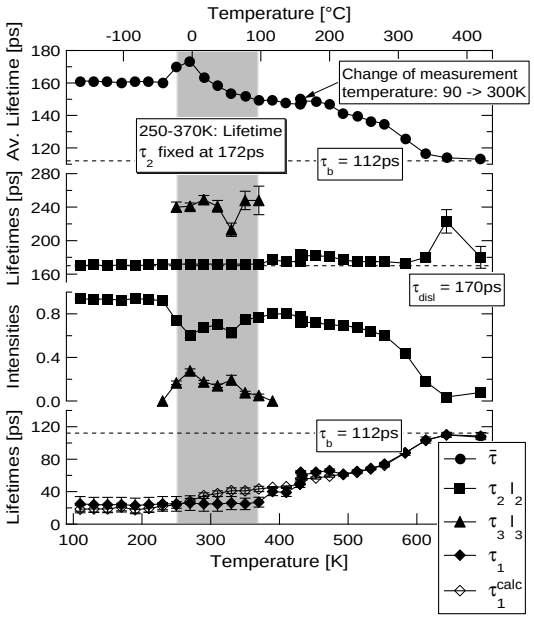


**Figure 5.** Annealing of a 2 MeV electron-irradiated sintered sample; the irradiation dose was $5 \times 10^{18}$ cm$^{-2}$. The figure gives the average lifetime (upper part), the decomposition of the spectra, and a comparison between the measured and calculated reduced bulk lifetime (lower part). Vacancies become mobile at about 220 K. Thereafter, vacancy clustering is observed.

with some 1–3% intensity, which could be due to an average grain size of about 12–15 $\mu$m.

There are certainly two types of defect generated by plastic deformation: dislocations and monovacancies due to dislocation intersection and jog dragging [31]. The movement of jogged screw dislocations is likely to create vacancies. The jog-generated vacancies are closely associated with the dislocation jog which generated them. They have a tendency to cluster [33, 34]. Vacancies in copper are mobile even below room temperature, and hence are likely to form clusters which can be detected after deformation. But since the positron lifetimes for dislocations (170 ps) and for vacancy clusters (210–300 ps) are very close for smaller clusters, it is difficult to decompose these spectra.

The three-component analysis of our lifetime spectra indicates dislocations and vacancy clusters as generated defects. The results for bulk copper are given in [9].

Utilizing the trapping model, we calculated the dislocation densities using equations given in [9] (and the trapping coefficient from table 4) and the reduced bulk lifetime $\tau_1^{\mathrm{calc}}$. We compared these with the measured ones. We found sufficient coincidence for smaller degrees of deformation (see also [9]).

While the cluster signal vanishes at about 120 °C, the dislocation signal vanishes—according to the degree of deformation—between 250 and 350 °C. Independently of which deformation mechanism was operative, all of the samples show, at 400 °C, nearly the bulk lifetime again [9]. This indicates that all defects detectable with positron lifetime spectroscopy have already annealed out, meaning that recrystallization is complete.

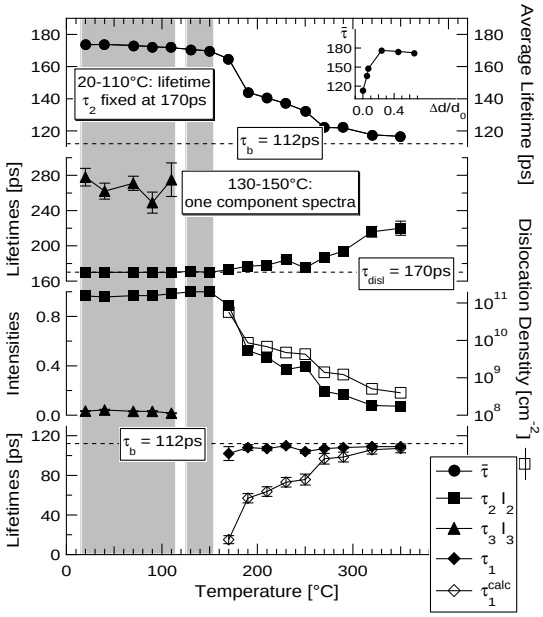


**Figure 6.** Plastically deformed ($\Delta d/d_0 = 0.66$) sintered samples (900 °C, 12 h); thickness reduction caused by pressing; vacancy clusters anneal out at about 100 °C. Thereafter, complete trapping into dislocations (the single-component spectrum) is observed for larger degrees of deformation. The lower part shows a comparison to the trapping model. The samples were annealed at each temperature point for 30 min under vacuum. The dislocation density drops from $\approx 1 \times 10^{11}$ (20–150 °C) to $3 \times 10^8$ cm$^{-2}$ (at 310 °C). The inset gives the change of the average lifetime with increasing degree of deformation.

**Table 4.** Positron data for copper determined in this work and according to the references given. The lifetimes for vacancies were determined in thermal equilibrium at 1110 K, '(thermal)', or after irradiation at 77 K, '(irradiated)', and the ones for dislocations ($\tau_{\rm disl}$) after cold rolling. The trapping coefficients given are for vacancies ($\mu_{\rm v}$) and dislocations ($\mu_{\rm disl}$).

| | Schaefer/ Hinode *et al* | Hehenkamp *et al* [19, 20] | Literature | Saoucha *et al* [24] | This work |
|---|---|---|---|---|---|
| $\tau_{\rm b}$ (ps) | 110 [25] | $111 \pm 2$ | 103–110 [21–23] | $111 \pm 2$ | $112 \pm 2$ ps |
| $\tau_{\rm v}$ (ps) (thermal) | 155 [25] | $158 \pm 1.5$ | — | — | — |
| $\tau_{\rm v}$ (ps) (irradiated) | 179 [25] | — | — | — | $170 \pm 1$ ps |
| $\tau_{\rm disl}$ (ps) | $176 \pm 6$ [26] | — | — | — | $170 \pm 2$ ps |
| $\mu_{\rm v}$ ($10^{14}$ s$^{-1}$) | | 1.3 | | — | — |
| $\mu_{\rm disl}$ (cm$^{-2}$) | | | $1.1 \pm 0.2$ [27, 28] | — | — |

*3.2.4. The annealing behaviour of uncompressed powder.* We investigated the annealing out of defects caused by the powder production process by making measurements on uncompressed powder.

(i) *Electrolytic copper powder.* The electrolytic copper powder was heated at a rate of 3 K min$^{-1}$ to 20, 200, 300, and 400 °C.

We choose this temperature range since at higher temperature sintering starts and the powder begins to solidify, and, hence, it will be difficult to make measurements on *powder*. The analysis of the defects detected shows, as seen in figure 7, that even the powder, as produced,

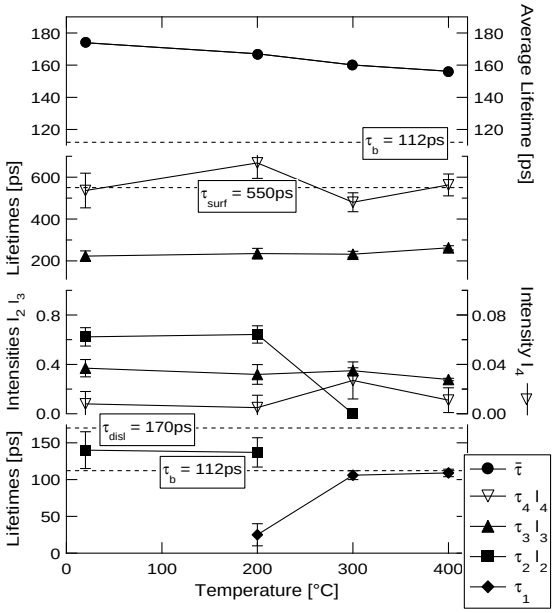


(a)

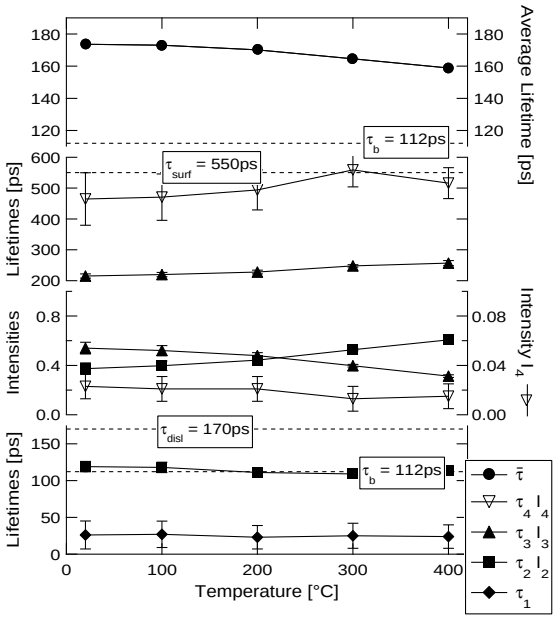


(b)

**Figure 7.** The annealing behaviour of uncompressed electrolytic (a) and spherical (b) copper powder. The powders were heated at a rate of 3 K $min^{-1}$ up to the temperatures indicated. The multi-component analysis reveals a surface component for each powder besides a vacancy-cluster-like lifetime and, for electrolytic powder, at lower temperatures, a dislocation lifetime. It is possible that the dislocation lifetime is not resolved for the spherical powder.

leads to nearly saturated trapping of the positrons. This means that there is a reduced bulk lifetime $\tau_1$ with a very small intensity, and, hence, one cannot determine any defect densities accurately—one can only give a lower limit. This will be done in section 3.4—in comparison to x-ray results. Vacancy-cluster-like signals are detected even at 400 °C and higher temperatures. Looking at the lifetime $\tau_2$, we realize that it changes upon heat treatment from a positron lifetime in dislocations of about 160 ps to the bulk lifetime. This indicates the annealing out of dislocations, and a subsequently defect-free interior for the grains. The two other lifetimes detected ($\tau_3 \approx 250$ ps, $\tau_4 \approx 550$ ps) can be attributed to positrons trapped at grain boundaries and at surfaces. Their intensities decrease as temperature increases. The surface component is due to positrons reaching the surfaces of powder particles. Their corresponding intensity increases slightly when the traps inside are partly annealed out.

(ii) *Spherical copper powder.* For the temperature range considered, there is only a slight decrease in the average lifetime. From the discrete lifetime analysis as well as from MELT (see [9] for details), we obtain four different lifetimes: $\tau_1 \approx 25$ ps, $\tau_2 \approx \tau_b = 112$ ps (200–400 °C), $\tau_3 \approx 230$ ps, and $\tau_4 \approx 550$ ps (the surface lifetime). The intensity $I_2$ is increased by heat treatment up to 400 °C, while $I_3$ decreases. This effect could be due to a small, unresolvable dislocation component ($\tau_{disl} = 170$ ps), which could influence both intensities and lifetimes [35].

Vacancy-cluster-like signals are detected even at 400 °C and higher temperatures. Looking at the lifetime $\tau_2$, we realize that we measured, following the heat treatment at higher temperature, an increasing intensity but always the bulk lifetime. The detection of a positron lifetime at surfaces sounds reasonable, due to the average particle size of about 19 $\mu$m, which includes a broad powder-particle size distribution (see section 2.2), so there are certainly enough smaller powder particles for there to be a specific fraction of positrons that have a good chance of reaching the surface [16].

*3.2.5. Comparison of different rates of heating.* We compare the positron lifetime data for compacts of electrolytic copper powder heated up at a rate of 10 K min$^{-1}$ and similar samples held at each of several temperatures for 30 min in the furnace. The average lifetime shows no clear difference from that for a heating rate of 10 K min$^{-1}$, but there is a difference from that for a heating rate of 50 K min$^{-1}$, indicating that during the cooling of the sample the heat-induced processes evolve further [9].

Hence, we can compare the shrinkage monitored *in situ* and, e.g., POLIS and metallographic data determined for quickly cooled samples (interrupted sintering) only if we keep in mind that in the latter case of high heating rates the processes will have evolved further during cooling.

### *3.3. TEM results*

Electrolytic copper samples, previously investigated by POLIS measurements (heating rate: 50 K min$^{-1}$), were investigated using TEM, and the following results have been published in [36].

The great advantages of TEM are that one can: locally observe the microstructure; carry out *in situ* experiments; and examine pressed compacts of powders with small powder-particle sizes. But it is rather difficult to prepare samples for TEM. The problem is that we do not know whether the conditions in the few cases in which powder particles were investigated were representative or not.

The powder-particle size was estimated from SEM and TEM to be 2 to 5 $\mu$m. The powder particles are found to be polycrystalline with about 1 $\mu$m crystallite size at the beginning of the

sintering process. This is in agreement with the metallographic studies of the same samples.

It was possible to distinguish between grain boundaries and contact boundaries, since the latter show an irregular structure in comparison to the former†. From 400 °C and at higher temperatures, twin boundaries are visible, indicating recrystallization. The 600 °C sample showed small pores, a few nm in size, on and near a contact boundary [36].

All of the samples investigated show *local* dislocation densities of about $10^8$–$10^9$ cm$^{-2}$. The dislocations are not homogeneously distributed; i.e. areas with high and low densities can be found. This is in agreement with positron results, indicating, for temperatures higher than 400 °C, a global dislocation density smaller than $2 \times 10^8$ cm$^{-2}$. For a more detailed discussion, see [36].

### *3.4. X-ray line-profile analysis*

Evaluating the line broadening of x-ray diffraction peaks can reveal information about lattice disorder of the second kind (dislocations, small- and large-angle grain boundaries, twins) in polycrystalline materials. Warren–Averbach analysis gives the x-ray domain size (the grain size if smaller than ≈0.5 $\mu$m, the subgrain size, or the distance of twins). The data are estimates extrapolated to smaller grain sizes if the values are near the lower limit of 0.5 $\mu$m. The Krivoglaz–Wilkens plot gives the dislocation densities (see [37] and references therein). A comprehensive discussion will be given in part II [38].

**Table 5.** Uncompacted electrolytic copper powder: x-ray domain sizes $D$ and dislocation densities $N_{\mathrm{disl}}$ estimated from x-ray line-profile analysis as well as dislocation densities $N_{\mathrm{disl}}$, powder-particle sizes $\bar{L}_{\mathrm{P}}$, and grain sizes $\bar{L}_{\mathrm{G}}$ estimated from POLIS data for uncompacted electrolytic copper powder heated at a rate of 3 K min$^{-1}$ up to the given temperatures.

| | X-ray diffraction | | POLIS | | |
|---|---|---|---|---|---|
| $T$ (°C) | $D$ ($\mu$m) | $N_{\mathrm{disl}}$ ($10^{11}$ cm$^{-2}$) | $\bar{L}_{\mathrm{P}}$ ($\mu$m) | $\bar{L}_{\mathrm{G}}$ ($\mu$m) | $N_{\mathrm{disl}}$ ($10^{11}$ cm$^{-2}$) |
| 20 | $\geqslant 0.5$ | $1.33 \pm 0.13$ | — | $\leqslant 0.7$ | $0.5 \pm 0.2$ |
| 200 | $> 0.5$ | $1.19 \pm 0.18$ | $6 \pm 3$ | $\approx 1$ | $0.2 \pm 0.05$ |
| 300 | $> 0.5$ | $0.4 \pm 0.1$ | $4 \pm 2$ | $\approx 1.3$ | $\leqslant 0.01$ |
| 400 | $> 0.5$ | $< 0.05$ | $5 \pm 2$ | $\approx 1.5$ | $< 0.003$ |

**Table 6.** Uncompacted spherical copper powder: dislocation densities $N_{\mathrm{disl}}$, powder-particle sizes $\bar{L}_{\mathrm{P}}$, and grain sizes $\bar{L}_{\mathrm{G}}$ estimated from POLIS data for uncompacted spherical copper powder heated at a rate of 3 K min$^{-1}$ up to the given temperatures.

| $T$ (°C) | $\bar{L}_{\mathrm{P}}$ ($\mu$m) | $\bar{L}_{\mathrm{G}}$ ($\mu$m) | $N_{\mathrm{disl}}$ ($10^{11}$ cm$^{-2}$) |
|---|---|---|---|
| 20 | $11 \pm 3$ | $0.4 \pm 0.2$ | $< 0.02$ |
| 100 | $11 \pm 3$ | $0.5 \pm 0.2$ | $< 0.01$ |
| 200 | $11 \pm 3$ | $0.6 \pm 0.2$ | $< 0.01$ |
| 300 | $12 \pm 3$ | $0.8 \pm 0.2$ | $< 0.005$ |
| 400 | $14 \pm 3$ | $1.0 \pm 0.3$ | $< 0.005$ |

For the uncompacted powder, we obtained the data given in table 5. The results from POLIS, estimated according to the model discussed in section 3.2, are included in table 5 for comparison. See also table 6 giving only POLIS data.

† The preparation of samples at lower temperatures was very difficult, due to poor mechanical stability.

**Table 7.** Compacts of electrolytic copper powder ($v_A = 50$ K min$^{-1}$): x-ray domain sizes $D$ and dislocation densities $N_{disl}$ estimated from x-ray line-profile analysis as well as grain sizes $\bar{L}_G$ and dislocation densities $N_{disl}$ estimated from metallography, TEM, and positron annihilation data for samples pressed and sintered up to the given temperatures. The maximum dislocation densities found by TEM were locally $\leqslant 10^9$ cm$^{-2}$ (400–900 °C).

| | X-ray diffraction | | Metallography | TEM | POLIS | |
|---|---|---|---|---|---|---|
| $T$ (°C) | $D$ ($\mu$m) | $N_{disl}$ ($10^{11}$ cm$^{-2}$) | $\bar{L}_G$ ($\mu$m) | $\bar{L}_G^{max}$ ($\mu$m) | $\bar{L}_G$ ($\mu$m) | $N_{disl}$ ($10^{11}$ cm$^{-2}$) |
| 20 | $0.29 \pm 0.15$ | $2.3 \pm 0.3$ | $\leqslant 2.4$ | — | $\leqslant 1.5$ | $> 0.8$ |
| 200 | — | — | — | — | $\leqslant 1.7$ | $> 0.5$ |
| 300 | $> 0.5$ | $0.61 \pm 0.2$ | — | — | $\leqslant 1.8$ | $0.15 \pm 0.05$ |
| 400 | — | — | — | $\approx 2$ | $\leqslant 2.0$ | $0.04 \pm 0.02$ |
| 600 | $> 0.5$ | $\leqslant 0.05$ | $\leqslant 2.4$ | $\approx 3$ | $\approx 2.2$ | $< 0.002$ |
| 800 | — | — | — | $\approx 5$ | $\approx 3$ | $< 0.002$ |
| 900 | $\gg 0.5$ | $< 0.05$ | $3.1 \pm 1.0$ | $\approx 8$ | $\approx 4$ | $< 0.002$ |
| 900 (30 min) | $\gg 0.5$ | $< 0.05$ | $5.4 \pm 1.5$ | $\approx 10$ | $\approx 6$ | $< 0.002$ |

**Table 8.** Compacts of spherical copper powder ($v_A = 10$ K min$^{-1}$): x-ray domain sizes $D$ and dislocation densities $N_{disl}$ estimated from x-ray line-profile analysis as well as grain sizes $\bar{L}_G$ estimated from metallography and positron annihilation data (also given: dislocation densities $N_{disl}$) for samples pressed and sintered up to the given temperatures. At higher temperatures (>400 °C), grain sizes determined by metallography are influenced by twin boundaries, while positrons are not sensitive to them, since twin boundaries are not open-volume defects.

| | X-ray diffraction | | Metallography | POLIS | |
|---|---|---|---|---|---|
| $T$ (°C) | $D$ ($\mu$m) | $N_{disl}$ ($10^{11}$ cm$^{-2}$) | $\bar{L}_G$ ($\mu$m) | $\bar{L}_G$ ($\mu$m) | $N_{disl}$ ($10^{11}$ cm$^{-2}$) |
| Powder | $> 0.5$ | $1.9 \pm 0.3$ | — | $\leqslant 1.0$ | $0.27 \pm 0.15$ |
| 300 | — | — | $4.9 \pm 1.0$ | $\approx 1.0$ | $0.82 \pm 0.3$ |
| 400 | $0.2 \pm 0.15$ | $1.3 \pm 0.2$ | $3.9 \pm 1.0$ | $\approx 1.0$ | $0.27 \pm 0.15$ |
| 500 | $0.37 \pm 0.3$ | $0.92 \pm 0.15$ | $5.1 \pm 1.0$ | $\approx 1.0$ | $0.12 \pm 0.05$ |
| 600 | $\geqslant 0.5$ | $0.48 \pm 0.12$ | $8.0 \pm 1.5$ | $4.0 \pm 1.0$ | $0.005 \pm 0.003$ |
| 800 | $\gg 0.5$ | $< 0.05$ | $10.1 \pm 2.0$ | $9.0 \pm 2.0$ | $\ll 0.003$ |
| 900 | $\gg 0.5$ | $< 0.05$ | $9.8 \pm 2.0$ | $10.0 \pm 2.0$ | $\ll 0.003$ |

For the pressed and sintered samples, the results are given in tables 7 and 8. The results from metallography as well as the grain sizes and dislocation densities estimated from the POLIS data, determined as described in section 3.2, are included for comparison.

The line-profile analysis for the 500 °C and the 600 °C compacts of spherical copper powder shows a large difference in the peak shape which is not reflected clearly in the data given in table 8. There could be two fractions of x-ray domains in the 600 °C sample.

## 4. Discussion

In this section we will discuss the complementary investigations (section 4.1), and then, with these results in mind, consider the consequences of the defect analysis for the sintering process. We will—in short—present a new analysis of data measured previously (see [9] for a detailed review). Section 4.2 contains the analysis of the data obtained from this work, and section 4.3 describes the consequences for sintering models.

### *4.1. The behaviour of defects under annealing*

*4.1.1. Electron-irradiated samples.* As discussed in section 3.2.2, vacancy clusters are formed as a result of low-temperature electron irradiation and subsequent annealing up to 220 K, whereupon monovacancies become mobile. The clusters anneal out at about 383 K (110 °C). Nevertheless, a vacancy-like signal ($\tau_2 \approx 174$ ps) seems to persist up to 700 K. This is perhaps due to the formation of prismatic dislocation loops by collapsing vacancy clusters. In the presence of excess vacancies, the dislocation loops are likely to grow by positive climbing due to capture of vacancies (see chapter 3.7 of [31]). If there is a vacancy sink in the vicinity, the loops will emit vacancies and shrink by negative climbing. At 350 °C we measured the bulk lifetime of copper again, indicating that the defect densities are below the limits given in [9].

*4.1.2. Plastic deformation and electron irradiation of sintered electrolytic copper samples.* While the cluster signal vanishes at about 120 °C, which is also the temperature at which clusters anneal out after electron irradiation, the dislocation signal vanishes—according to the degree of deformation—between 250 and 350 °C ($\approx$0.4 $T_M$). At 400 °C all of the samples—independently of the mechanism of deformation that was operative and the degree of deformation—show nearly the bulk lifetime again; this indicates that all defects detectable by means of positron lifetime spectroscopy have recovered; i.e. their values are below the sensitivity limits of positron annihilation given in [9]. This is qualitatively the same as what is observed for the similarly treated pure metal samples [9]. The astonishing fact—considering that there is the same degree of deformation—that recovery and recrystallization take place at lower temperatures in these less pure samples can be explained by the small grain sizes. From the MC simulation of the positron diffusion, we can estimate the average grain size to be about 15 $\mu$m, since for nearly all of these samples there was a small vacancy-cluster component detectable after annealing and before deformation. Since we know from the annealing of electron-irradiated samples that vacancy clusters anneal out at about 110 °C (the samples were heat treated at 900 °C for several hours), this signal can only stem from large-angle grain boundaries which are acting after deformation and during annealing as vacancy sources and sinks, and, hence, are enhancing the diffusion-controlled recovery and recrystallization processes (this view is confirmed by the metallographic studies). In view of the comparable grain sizes, recovery and recrystallization should occur earlier for the compact copper samples with higher purity.

*4.1.3. Reinterpretation of former results.* In earlier studies of the sintering process by positron lifetime spectroscopy [5, 6, 39, 40], independently of the green density or heating rate, a coincidence of the decreasing average lifetime $\bar{\tau}$ and intensive-shrinkage stage was observed (see [9]). These studies revealed an unusually high average lifetime—i.e. 20–30 ps higher than after massive plastic deformation (complete trapping)—after e.g. 50% cold rolling. Additionally, an increase of the average lifetime at about 0.4 $T_M$ was noticed, which seems to be contrary to the results presented here. But it has been shown in [9] that this contradiction can be resolved as follows.

The often-observed increase in the average lifetime prior to the intensive-shrinkage stage could be explained by nearly complete trapping into defects before and after recrystallization. If such an assumption was valid, and one type of defect with a comparatively small lifetime ($\tau_{disl} = 155$–$170$ ps) is being annealed out while other defects with longer lifetimes ($\tau_{GB} \approx 250$ ps, $\tau_{surf} \approx 550$ ps) survive, then the average lifetime will increase even though some defects anneal out [9].

We see that the observation of increasing $\bar{\tau}$ during recrystallization and a decrease of $\bar{\tau}$ due to grain growth and elimination of pore space, when the sintering is starting, is generic to the earlier work. The powders considered in this work do not have a sponge-like morphology or such a fine-grained microstructure as those considered in the earlier work. Hence, recrystallization leads to an annealing stage (decrease of $\bar{\tau}$), because complete trapping is not observed. The further decrease of $\bar{\tau}$ during the intensive-shrinkage stage has the same cause as in the earlier work: elimination of pore surfaces and grain growth.

### *4.2. The behaviour of defects during sintering*

As regards the sintered samples, we can say that compacts of both powders show very complicated defect structure for temperatures below 600 °C. In this temperature range, it is likely that deformation-generated defects such as dislocations, possibly small-angle grain boundaries, and vacancy clusters have not yet annealed out.

One important fact is that the prevailing part of the shrinkage is realized during the heating of the sample, i.e. when recrystallization is completed and the grain growth is starting at the higher temperatures.

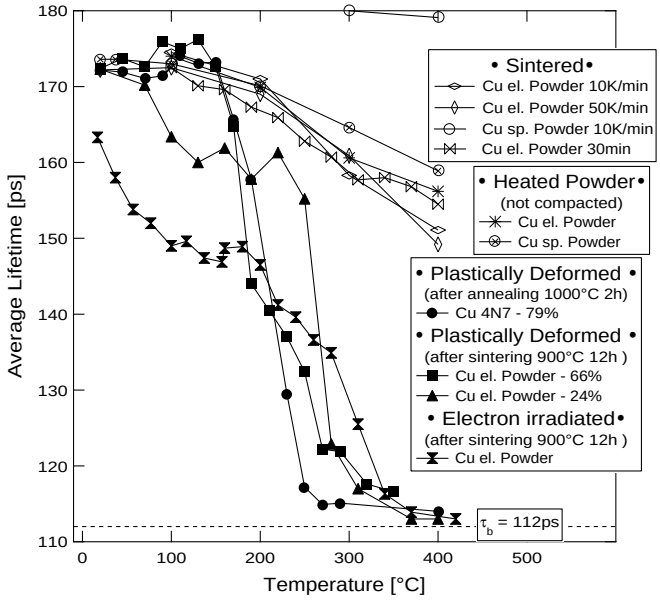


**Figure 8.** The annealing behaviour up to 400 °C for all of the differently treated samples. Note that there are only minor differences between the annealing behaviours of uncompacted and compacted powders, while defects caused by electron irradiation and those generated by plastic deformation have annealed out totally at about 400 °C.

From comparison to the average lifetimes of deformed and irradiated samples shown in figure 8, it can be clearly seen that above 400 °C, in powders or compacts, defects other than monovacancies, vacancy clusters, and dislocations must lead to the observed average lifetimes, which are well above the bulk value. Note the small differences in annealing behaviour between the heated powder and pressed samples.

For temperatures higher than 600 °C, there are—besides a small surface component for electrolytic copper—only two main lifetime components detectable for sintered samples: the

bulk lifetime and a positron lifetime, as for vacancy clusters, i.e. $\tau_1 \approx \tau_b$ and $\tau_2 \approx \tau_{cl} \approx$ 300 ps—corresponding to about eight vacancies [17]. But since vacancy clusters are not likely to exist at such a high temperature, only large-angle grain boundaries, i.e. with grain sizes below ≈15 $\mu$m, can explain the result. This means that defect-free grains of size smaller than about 15 $\mu$m exist, where $\tau_1 \approx \tau_b$ due to annihilation in the recrystallized interior of the grains, while $\tau_2$ should be ≈300 ps due to capture of the positrons at the grain boundaries and subsequent annihilation. The results given in tables 7 and 8 show an increasing grain size with increasing temperature, detected by different methods.

Compacts of spherical powder show a different annealing behaviour in comparison to compacts of the electrolytic powder. But the lifetime results are consistent with the changes in the microstructure shown by metallography and x-ray diffraction (see table 8). As shown in figure 4, the drastic fall of the average lifetime $\bar{\tau}$ from 500 to 600 °C—accompanying a significant change in the microstructure of the samples—is caused by the vanishing of the positron lifetime component corresponding to dislocations (≈170 ps). Since the lifetime signal due to dislocations usually vanishes after plastic deformation between 250 and 350 °C (≈0.4 $T_M$; see section 3.2.3), this effect can probably be attributed to subgrain coalescence due to subgrain rotation and subgrain growth [41]. This assertion is supported by x-ray domain sizes of 0.37 ± 0.3 $\mu$m at 500 and ⩾0.5 $\mu$m at 600 °C. The x-ray domain size can be a subgrain size (see section 3.4). For temperatures higher than 600 °C, only two separate lifetime components are detected (see above). But the intensity $I_2$ ($\tau_2 \approx \tau_{cl}$) is lower than at comparable temperatures for electrolytic powder (see figures 3 and 4).

There are possibly systematic errors in the grain sizes determined by metallography, in that very small grains are not visible if one is using an optical microscope.

Where they can be determined quite certainly, the dislocation densities determined by means of x-ray diffraction and POLIS differ by a factor of roughly 5. There could be a difference between the POLIS sensitivity for dislocations in the volume and that for those arranged in subboundaries.

The shrinkage rate reaches its maximum for compacts of both powders and heating rates when lifetime spectroscopy indicates that there are defect-free grains and that positrons are trapped exclusively at grain boundaries, i.e. above 0.4 $T_M$ (see figures 3 and 4). The rates of change in the microstructure are different for the sintered compacts of the two powders between 500 and 700 °C. The rate is much smaller for compacts of electrolytic powder. This could be due to the very inhomogeneous powder-particle size distribution.

*4.2.1. Uncompacted powder.* To confirm the hypothesis of a defect-free interior of grains and trapping at the boundaries, we can look at the results for powders not pressed prior to heat treatment: the nearly saturated trapping observed in uncompressed electrolytic copper powder has two possible causes: on the one hand, there could be very high densities of dislocations and vacancy clusters in the volume; or, on the other hand, there could be trapping at grain boundaries (large and small angle) due to the material being very fine grained. These cases can be distinguished by considering the annealing kinetics. Vacancy clusters in the volume anneal out at approximately 383 K (110 °C) (see section 3.2.2) while dislocations with high densities should anneal out below approximately 600 K (300 °C) (see section 3.2.3). But since vacancy-cluster-like signals are detected even at 400 °C (and also at higher temperatures—consider pressed samples), these signals can only stem from large-angle grain boundaries due to a fine-grained structure of the material; the grain size at 400 °C can be estimated to be 1–2 $\mu$m. This assertion is strongly supported by the defect analysis of electrolytic powder annealed at 20 and 200 °C. We detect only two positron lifetimes for defects of about 160 ps and 300 ps, which could be attributed typically to small- and large-angle grain boundaries. At

higher temperatures the reduced bulk lifetime becomes $\tau_1 = 112$ ps (the bulk lifetime for well annealed samples). The results are in accordance with x-ray diffraction data, since we see in table 5 that the measured x-ray domain sizes are never smaller than 0.5 $\mu$m, in agreement with lifetime data.

*4.2.2. Consequences for sintering.* The only explanation for such a defect characteristic, i.e. that the reduced bulk lifetime always equals the bulk lifetime, is that there are regions in the material investigated which are nearly free of defects that affect positrons, leading to the measured bulk lifetime, and high defect densities in other parts, leading to the measured defect-related lifetimes. One possible candidate scenario is a cellular-structure-like defect-free interior of grains in the powder particles. Since positrons which thermalize inside the grains, supposed to be free of defects, do not 'see' any defects on their diffusion path, the annihilation rate should be that of the bulk. 'Inside the grain' means far from the boundaries as compared to the diffusion length of approximately 330 nm (see the discussion in section 3.2).

Hence, we seem to be monitoring, for temperatures above 600 °C, by means of the vacancy-cluster-like positron lifetime and its intensity, initially the grain growth inside the powder particles, and later that in the sintered body.

### *4.3. Possible sintering mechanisms*

The three possible creep mechanisms which will be discussed below can contribute at different temperatures different fractions to the total shrinkage. It seems unlikely that only one mechanism will contribute to the sintering at different temperatures.

Considering intermediate-stage sintering, for all of the different transport mechanisms the driving force $\sigma$ for pressureless sintering of porous samples is given by the *Laplace pressure* (see [42], chapter 2.2)

$$\sigma = A_0 \frac{2\gamma_S - \gamma_{GB}}{\bar{L}_P} \Theta \tag{1}$$

acting as a capillary tension, where $\gamma_S$ and $\gamma_{GB}$ are the surface and grain boundary energy, respectively, $\bar{L}_P$ is the average powder-particle size, $\Theta$ is the porosity, and $A_0$ is a number ($1, \ldots, 4$, according to the particle geometry, where $A_0 = 4$ for spherical particles). Equation (1) is suitable for describing the driving force during the intermediate stage. But it is questionable whether it describes the driving force accurately for the small curvature radii at the initial stage.

For *Nabarro–Herring* and *Coble* creep, the estimated shrinkage rates are given by

$$\dot{\varepsilon}_{NH} = A_1 \frac{D_{vol}\Omega\sigma}{k_B T} \frac{1}{\bar{L}_G^2} \tag{2}$$

and

$$\dot{\varepsilon}_C = A_2 \frac{\delta_{GB} D_{GB}\Omega\sigma}{k_B T} \frac{1}{\bar{L}_G^3} \tag{3}$$

respectively, while for dislocation creep we have

$$\dot{\varepsilon}_{disl} = A_1 \frac{N_{disl} D_{vol}\Omega\sigma}{k_B T} = A_1 \frac{D_{vol}\Omega\sigma}{k_B T} \frac{1}{\bar{L}_{disl}^2} \qquad \bar{L}_{disl} = \left[\sqrt{N_{disl}}\right]^{-1} \tag{4}$$

where $\bar{L}_G$ is the average crystallite size, and $D_{vol}$ and $D_{GB}$ are the volume and grain boundary diffusion coefficients, respectively; $A_1$ and $A_2$ are empirical constants, $\Omega$ is the atomic volume,

$\sigma$ the external or internal (porous-body) tension, $\delta_{GB}$ the effective grain boundary width, $N_{disl}$ the movable dislocation density, $k_B$ the Boltzmann constant, and $T$ the absolute temperature.

For dislocation creep dominating over Nabarro–Herring creep, it is required for the dislocation density $N_{disl}$ that

$$N_{disl} > \left(\frac{1}{\delta \bar{L}_G^2}\right)^{2/3} \tag{5}$$

where $\delta \approx 10$ atomic diameters is the characteristic distance between a dislocation and a vacancy for which a vacancy will be absorbed [8]. Equation (5) expresses the requirement that dislocations dominate over grain boundaries as sources and sinks for vacancies [42], i.e. dislocation creep leads to larger shrinkage rates than Nabarro–Herring creep.

Alternatively, one can use a two-particle model modified to include flattening of powder particles by pressing [43–45]. This model is most appropriate for spherically shaped powders (see figure 9). It estimates the shrinkage rate from the experimentally measured shrinkage by equating the fraction of volume taken away at the contact boundary ($V_1$) and transported towards the neck ($V_2$), which gives an expression for the neck curvature $\rho$. Taking into account

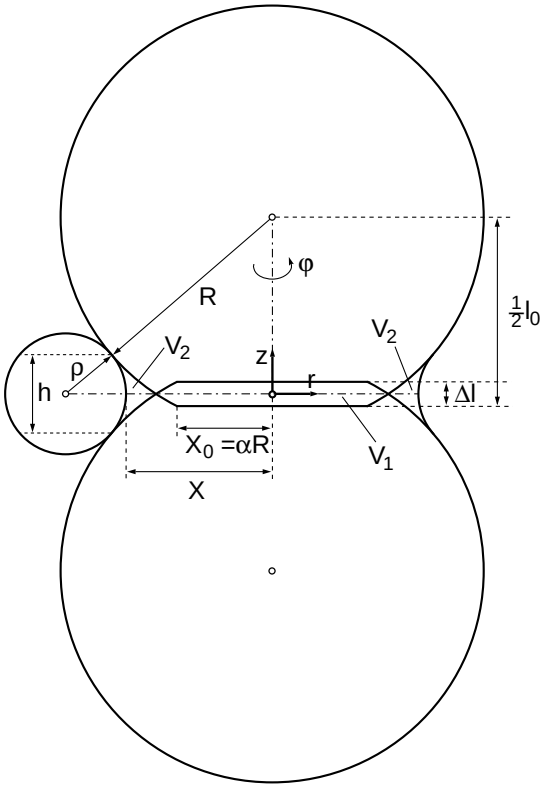


**Figure 9.** The modified two-particle model; for determination of the geometric activity. When $R$ is the original powder-particle radius, one can see the flattening of the two-particle contact caused by pressing, where $\alpha$ is the so-called *initial flattening*. Here, $X_0$ and $l_0$ are the neck radius and the particle distance, respectively, after pressing. Material transport causes the volume $V_1$ to migrate to the neck region where it is deposited ($V_2$). Hence, the outer neck radius $\rho$, the inner neck radius $X$, and the neck heights $h$ are enlarged. Simultaneously, the separation of the particle centres decreases by $\Delta l$. $r$, $\varphi$, $z$ are cylindrical coordinates used for the calculations.

Fick's law and appropriate boundary conditions, one is led to an equation for the shrinkage rate. The boundary conditions are: (i) the vacancy concentration near the neck is above the equilibrium value due to the principal radii of curvature ($\rho$, $X$) (see the Kelvin–Thompson equation) and (ii) the sintering neck must be free of tension $\sigma$, i.e. $2\pi \int_0^X \sigma r \, \mathrm{d}r = 0$, leading to a vacancy concentration in the middle of the sintering neck which deviates by the same amount from the equilibrium value as at the neck surface, but with the opposite sign [45, 46]. Taking

$$l_0 = 2R\sqrt{1-\alpha^2}$$

as the starting length ($R$ is the powder-particle radius and $\alpha = X_0/R$ is the flattening after pressing where $X_0$ is the initial neck radius), one obtains for the shrinkage rate

$$\frac{\mathrm{d}}{\mathrm{d}t}\left(\frac{\Delta l}{l_0}\right) = 2\left\{-\exp\left[-\frac{\Omega\gamma_S}{k_B T}\left(\frac{1}{\rho}-\frac{1}{X}\right)\right] + \exp\left[\frac{\Omega\gamma_S}{k_B T}\left(\frac{1}{\rho}-\frac{1}{X}\right)\right]\right\}\frac{1}{X^2 R\sqrt{1-\alpha^2}}\int_{-h/2}^{h/2} D_{\mathrm{eff}}(t,z)\,\mathrm{d}z \tag{6}$$

in an exact form, i.e. without the usual approximations $\Omega\gamma_S \ll k_B T$ and $\rho \ll X$. Since we solve the problem numerically, the validity range of the model in comparison to that of the original version [44] is increased [45]. In the case of relaxed boundaries, one obtains for the integral part of equation (6), involving an effective diffusion constant (see figure 10),

$$\int_{-h/2}^{h/2} D_{\mathrm{eff}}(t,z)\,\mathrm{d}z = D_{\mathrm{vol}}(h-\delta_{\mathrm{GB}}) + \delta_{\mathrm{GB}} D_{\mathrm{GB}} \tag{7}$$

which has been used in this work.

To determine which mechanism is dominant, we have to estimate an *influence zone* around the contact boundaries. In this zone, plastic deformation due to pressing will occur, and it is that very volume which can be influenced by self-activation of dislocations [42]. If one takes as the influence zone the half-sphere above the neck of a two-particle contact, then it is easily established that the volume fraction is independent of the powder-particle size. For the green densities considered here, it will be roughly one third of the total volume [45]. If there exist dislocation densities of some $10^9$ cm$^{-2}$, then this should be reflected in the POLIS data.

But since no indications of dislocations of sufficient density are found for the samples at the relevant temperature above 0.4 $T_M$, we can exclude the possibility of dislocation creep (equation (4)) being the relevant creep mechanism.

For calculating the shrinkage rates given in figures 11 and 12 according to the equations given above, we estimate the powder-particle ($\bar{L}_P$) and grain sizes ($\bar{L}_G$) according to the positron data, which are in accordance with those collected by other methods (see tables 2, 3, 7, and 8). The constant $A_0$ should be smaller than 4 due to the deviations of the shapes of the powder particles from spherical, but the choice of $A_0 = 3$ is deliberate, to get the right maximum of the shrinkage rate. In the following we give the relevant constants taken from [47]: the Boltzmann constant $k_B = 8.617\times10^{-5}$ eV K$^{-1}$; the volume diffusion coefficient $D_{\mathrm{vol}} = D_0^{\mathrm{vol}}\exp(-Q_{\mathrm{vol}}/k_B T)$ ($D_0^{\mathrm{vol}} = 0.62 \times 10^{-4}$ m$^2$ s$^{-1}$, $Q_{\mathrm{vol}} = 2.12$ eV); the grain boundary diffusion coefficient $D_{\mathrm{GB}} = D_0^{\mathrm{GB}}\exp(-Q_{\mathrm{GB}}/k_B T)$ ($D_0^{\mathrm{GB}} = 0.1 \times 10^{-4}$ m$^2$ s$^{-1}$, $Q_{\mathrm{GB}} = 1.06$ eV); the surface tension $\gamma_S = 1.721$ J m$^{-2}$; the grain boundary tension $\gamma_{\mathrm{GB}} = 0.625$ J m$^{-2}$; the atomic volume $\Omega = 1.18 \times 10^{-29}$ m$^3$; the effective cross section of grain boundary diffusion $\delta_{\mathrm{GB}} = 5.1 \times 10^{-10}$m; and the geometric constants $A_0 = 1, \ldots, 4$, $A_1 \approx 10$, $A_2 \approx 150$ from [42], while the porosity $\Theta$ is calculated from shrinkage data.

Considering figure 11, we see that, by using our very simple model for positron diffusion and annihilation (see section 3.2), with the rough estimates for the effective powder-particle size

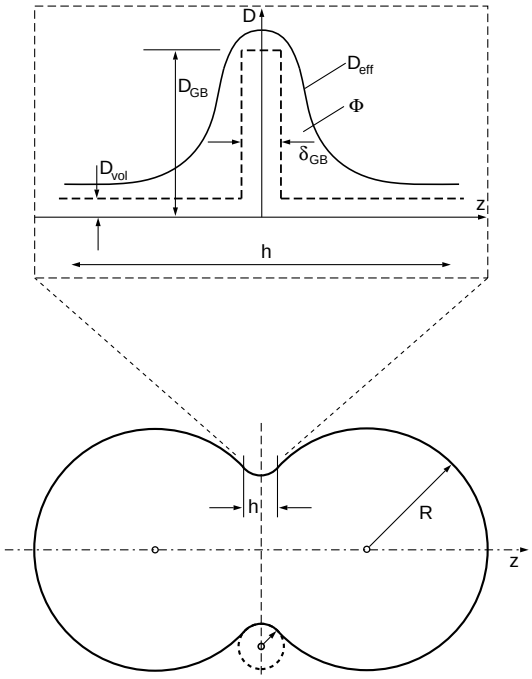


**Figure 10.** The modified two-particle model; the lower part gives the geometry of the powder particles, while the upper part shows the course of the diffusion coefficient enlarged along the neck radius. The structural activity $\Phi$ is the area below the curve of the effective diffusion coefficient $D_{\mathrm{eff}}$ ($D_{\mathrm{vol}}$ and $D_{\mathrm{GB}}$ are the coefficients for volume and grain boundary diffusion, respectively, while $\delta_{\mathrm{GB}}$ is the effective grain boundary width). The profile for defect-free powder particles and relaxed grain boundaries is the dashed line, i.e. for $T > T_{\mathrm{R}} = 0.4\ T_{\mathrm{M}}$. The other symbols have been explained in figure 9.

and average grain size, Nabarro–Herring creep (equation (2)) leads to shrinkage rates that are too low, while Coble creep (equation (3)) gives nearly the right shrinkage rates. The shrinkage rate estimated from the dislocation creep is not given, since from the positron results the dislocation density above 500 °C is globally less than $2 \times 10^8$ cm$^{-2}$, and hence equation (5) is, for the given grain sizes (see table 7 and [42]), not obeyed. Even for the maximum dislocation densities estimated by means of TEM, equation (5) is only approximately obeyed between 800 and 900 °C [36]. Hence, we have not included dislocation creep in figure 11, since the shrinkage rate estimated using that model will be not much higher than that given by considering Nabarro–Herring creep. Since the process parameters are not known exactly and the models describe reality inside the compact only very roughly, one cannot expect an exact coincidence.

The two-particle model given by Lányi, assuming spherically shaped powders, is not applicable to the electrolytic powder, because of the irregular shape of the powder particles.

The shrinkage rate of the spherical copper powder compacts has been calculated also according to the modified two-particle model, i.e. according to equations (6) and (7), since this powder is suited as a model substance for spherical particles. This is more appropriate for this powder, since Nabarro–Herring (equation (2)) and Coble creep (equation (3)) underestimate the driving force due to the small curvature gradients at the necks. In the modified two-particle model, Coble creep dominates over Nabarro–Herring creep by at least a factor of 3 as

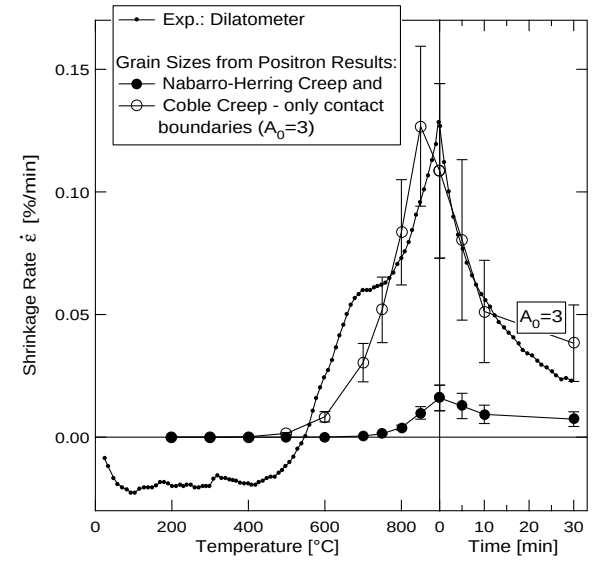


(a)

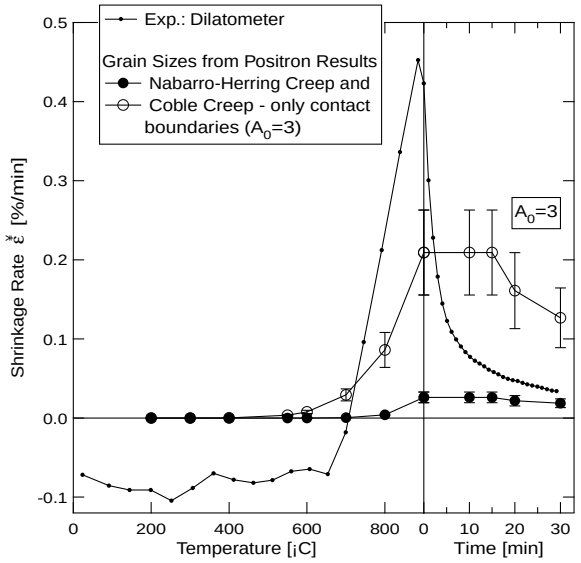


(b)

**Figure 11.** Shrinkage rates for different mechanisms as estimated from experimental results given for compacts of electrolytic copper powder for heating rates of 10 K $\text{min}^{-1}$ (a) and 50 K $\text{min}^{-1}$ (b); due to the irregular powder-particle shapes, we took as the geometry factor $A = 3$ (instead of $A = 4$ which is for spherical shapes), hence reducing the driving force. The calculations were carried out using the estimated grain and powder-particle sizes (see the text).

well. Figure 12 shows sufficient coincidence between the measured and calculated shrinkage rate, since the aim of this study was only to show which mechanism can best explain the high shrinkage rates observed experimentally. It was not intended to give a quantitative coincidence, since the models used are too simple.

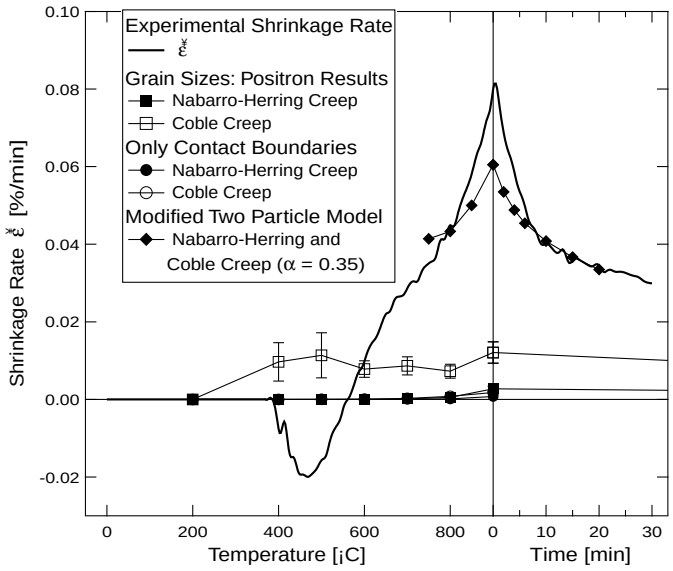


**Figure 12.** Compacts of spherical copper powder; we calculated the shrinkage rate due to the dilatometrically determined shrinkage according to the modified two-particle model (see the text). The heating rate was 10 K min$^{-1}$. At the sintering temperature, the relative contribution of the grain boundary diffusion is three times that of the volume diffusion. Please note that the symbols for NH creep and Coble creep (only contact boundaries) superimpose.

## 5. Conclusions

It is definitely possible to freeze a certain sinter stage by heating a sample up to a certain temperature and then quickly removing it from the furnace if the heating rate is not higher than approximately 10 K min$^{-1}$. For, e.g., 50 K min$^{-1}$ and even higher heating rates, one has to consider the possibility that some process is proceeding during cooling. Since most processes have an exponential temperature dependence, this effect will be small.

We showed that it is possible to monitor defects accompanying pressureless sintering processes in compacts of metal powders if one combines positron annihilation spectroscopy with other methods. However, one has to keep track of how far the lifetime analysis can be influenced by very small grain and powder-particle sizes. It was essential to apply the results of the Monte Carlo simulation of the positron diffusion and hence obtain an estimate of to what extent the lifetime data could stem from grain boundaries with a certain grain size (compared to the result determined by metallographic studies).

It is obvious that for temperatures higher than 500 °C, there should be no defects (dislocations or vacancy clusters) present at considerable densities in the sinter material, since we showed by comparison with the annealing behaviour of plastically deformed and electron-irradiated samples† that for all of these samples no defects were detectable for temperatures higher than 400 °C. At this temperature, the sintering process has not yet started. Hence, what we are monitoring at temperatures above 500 °C by means of positron annihilation must be large-angle grain boundaries, and thus, as indicated by the decreasing signal, grain growth. This is due to the two-component positron signal, where the first component is the lifetime in

† The high-purity copper samples and the sintered samples were heat treated before irradiation and deformation so that no (or nearly no) defects were measurable using positrons.

an undisturbed crystal (the interior of the grains) and the second one must stem from the grain boundaries. This is plausible, since there is a good qualitative correlation between the grain sizes estimated from positron data and metallography.

This interpretation of the POLIS data conforms with a new analysis of spectra taken previously. The differences from the results obtained in this work resulted from the different morphologies of the powders used.

The determination of powder-particle size and average grain size along with the defects detected by positron lifetime spectroscopy provide the parameters to use when considering the different proposed shrinkage mechanisms. Considering simply the different shrinkage mechanisms, one is led to the conclusion that Coble creep dominates the material transport in the systems investigated. The degree of dominance over pure volume diffusion decreases with increasing effective powder-particle size. Dislocation creep was ruled out for the systems investigated—at least if we consider an effective powder-particle size, i.e. the influence of agglomeration or irregular powder-particle shapes.

The modified two-particle model, taking into account the flattening of powder particles during pressing, is suited for describing the shrinkage rate for compacts of spherical powders. Even here, material transport due to Coble creep played the dominant role.

Powders suited for sintering seem to possess, above all, a very small effective powder-particle size, and hence a sufficient density of sources and sinks for vacancies. A very fine-grained structure inside each powder particle and very high dislocation densities can influence the material transport only if the distances between the sources and sinks become smaller than the influence zone of the Laplace tension (double the curvature of the neck).

## Acknowledgments

We would like to thank Professor W Schatt and Dr K-P Wieters (both at TU Dresden) for many interesting discussions, W Zeiger (TU Dresden) for the preparation of the sintered samples (part of his diploma thesis work), Dr F Dworschak (KFA Jülich) for preparing the electron-irradiated samples, Ch Nagel (University of Kiel) for preparing the source–sample sandwich and performing the low-temperature lifetime measurements of the electron-irradiated samples, Dr Carsten Böhme (TU Dresden) for supplying us with the spherical copper powder and for its particle-size analysis, Dr Hase and Dr C Blank for their support during the metallographic preparation at the TU Dresden, and Dr G Lange and Professor P Klimanek (both at Bergakademie Freiberg) for investigating some of the samples by means of x-ray diffraction and providing us with the results.

## References

[1] Kuczynski G C 1949 Self-diffusion in sintering of metallic particles *Trans. AIME* **185** 169–78
[2] Kuczynski G C 1950 Measurement of self-diffusion of silver without radioactive tracers *J. Appl. Phys.* **21** 632–5
[3] Rockland J G R 1967 The determination of the mechanism of sintering *Acta Metall.* **15** 277–86
[4] Schatt W, Arzt E, Friedrich E and Scheibe A 1986 Sintermechanismen für die Internsivschwindung in einphasigen Systemen *Z. Metallk.* **77** 228–33
[5] Schatt W and Hinz M 1988 On the generalizability of defect-activated sintering *Powder Metall. Int.* **20** 17–20
[6] Krause R, Schatt W, Vetter B and Polity A 1990 Study of sintering processes in copper and nickel by positron annihilation *Cryst. Res. Technol.* **25** 819–25
[7] Schatt W and Boiko J I 1991 Defektmechanismen des Schwindungsintensivstadiums *Z. Metallk.* **82** 527–31
[8] Geguzin Ja E 1973 *Physik des Sinterns* 1st edn (Leipzig: VEB Deutscher Verlag für Grundstoffindustrie)
[9] Staab T E M, Krause-Rehberg R and Kieback B 1999 Positron annihilation in fine-grained materials and fine powders—an application to sintering of technically used metal powders *J. Mater. Sci.* at press

[10] Schultz P J and Lynn K G 1988 Interaction of positron beams with surfaces, thin films and interfaces *Rev. Mod. Phys.* **60** 701–79
[11] Puska M J and Nieminen R M 1994 Theory of positrons in solids and on solid surfaces *Rev. Mod. Phys.* **66** 841–97
[12] Seeger A 1974 The study of defects in crystals by positron annihilation *Appl. Phys.* **4** 183–99
[13] Frank W and Seeger A 1974 Theoretical foundations and extensions of the trapping model *Appl. Phys.* **3** 61–6
[14] Hautojärvi P 1979 *Positrons in Solids (Springer Topics in Current Physics vol 12)* 1st edn (Berlin: Springer)
[15] Brandt W and Dupasquier A (ed) 1983 *Proc. Int. 'Enrico Fermi' School of Physics on Positron Solid State Physics* (Amsterdam: North-Holland)
[16] Hübner Ch, Staab T and Krause-Rehberg R 1995 Positron diffusion in fine-grained materials—a Monte Carlo simulation *Appl. Phys.* A **61** 203–6
[17] Staab T E M, Petters K, Hübner C G and Polity A 1999 Multi-component positron lifetime analysis of the annealing behaviour in electron irradiated and plastically deformed high-purity metals, at press
[18] Staab T E M, Somieski B and Krause-Rehberg R 1996 The data treatment influence on the spectra decomposition in positron lifetime spectroscopy; part 2: The effect of source corrections *Nucl. Instrum. Methods* A **381** 141–51
[19] Hehenkamp Th, Kurschat Th and Lühr-Tanck W 1986 Positron lifetime spectroscopy in copper *J. Phys. F: Met. Phys.* **16** 981–7
[20] Kluin J E and Hehenkamp Th 1991 Comparison of positron-lifetime spectroscopy and differential dilatometric measurements of the equilibrium vacancies in copper and $\alpha$-Cu–Ge alloys *Phys. Rev.* B **44** 597–608
[21] Jensen K O 1989 Local density calculations of positron annihilation in metals *J. Phys.: Condens. Matter* **1** 10 595–602
[22] Puska M J 1991 *Ab initio* calculations of positron annihilation rates in solids *J. Phys.: Condens. Matter* **3** 3455–69
[23] Sterne P A and Kaiser J H 1991 First-principles calculations of the positron lifetime in solids *Phys. Rev.* B **43** 13 982–98
[24] Saoucha A, Pedersen N J and Eldrup M 1992 On source contributions to positron lifetime spectra *Mater. Sci. Forum* **105–110** 1971–5
[25] Schaefer H E 1987 Investigation of thermal equilibrium vacancies in metals by positron annihilation *Phys. Status Solidi* a **102** 47–65
[26] Hinode K, Tanigawa S and Doyama M 1976 Positron lifetimes in deformed copper *J. Phys. Soc. Japan* **41** 2037–42
[27] Dlubek G, Brümmer O, Meyendorf N, Hautojärvi P, Vehanen A and Yli-Kauppila J 1979 Impurity-induced vacancy clustering in cold-worked nickel *J. Phys. F: Met. Phys.* **9** 1961–73
[28] Dlubek G, Krause R, Brümmer O, Michno Z and Gorecki T 1987 Impurity-induced vacancy clustering in cold-rolled nickel alloys as studied by positron annihilation techniques *J. Phys. F: Met. Phys.* **17** 1333–47
[29] Nieminen R M 1983 Defect and surface studies with positrons *Proc. Int. 'Enrico Fermi' School of Physics on Positron Solid State Physics* ed W Brandt and A Dupasquier (Amsterdam: North-Holland) pp 359–407
[30] Soininen E, Huomo H, Huttunen P A, Mäkinen J, Vehanen A and Hautojärvi P 1990 Temperature dependence of positron diffusion in cubic metals *Phys. Rev.* B **41** 6227–33
[31] Hull D and Bacon D J 1984 *Introduction to Dislocations* 3rd edn (Oxford: Pergamon)
[32] Fluss M J, Smedskjaer L C, Siegel R W, Legnini D G and Chason M K 1980 Positron annihilation measurement of the vacancy formation enthalpy in copper *J. Phys. F: Met. Phys.* **10** 1763–74
[33] Byrne J G 1979 A review of positron studies of the annealing of the cold worked state *Metall. Trans.* A **10** 791–807
[34] Nabarro F R N 1976 *Theory of Crystal Dislocations* (Oxford: Oxford University Press)
[35] Somieski B, Staab T E M and Krause-Rehberg R 1996 The data treatment influence on the spectra decomposition in positron lifetime spectroscopy; part 1: On the interpretation of multi-component analysis studied by Monte Carlo simulated model spectra *Nucl. Instrum. Methods* A **381** 128–40
[36] Hübner C G, Staab T and Leipner H S 1995 TEM studies of the microstructure of pressureless sintered copper *Phys. Status Solidi* a **150** 653–60
[37] Klimanek P 1992 Röntgendiffraktometrische Subgefügeanalyse an realen Vielkristallen *Habilitation* TU Bergakademie Freiberg
[38] Staab T E M, Krause-Rehberg R, Vetter B, Kieback B, Lange G and Klimanek P 1999 The influence of microstructure on the sintering process in crystalline metal powders investigated by positron lifetime spectroscopy: II. Tungsten powders with different powder-particle sizes *J. Phys.: Condens. Matter* **11** 1787
[39] Vetter B 1991 Korrelation von Schwindung/Schwindungsgeschwindigkeit und Materialtransportmechanismen

beim Sintern verschiedenartiger Einkomponentensysteme *PhD Thesis* Technische Universität Dresden

[40] Brand K 1993 Zum Einflußder Interdiffusion auf die Verdichtung beim Festphasensintern von Zweikomponentensystemen mit vollständiger Löslichkeit der Komponenten *PhD Thesis* Technische Universität Dresden

[41] Li J C M 1962 Possibility of subgrain rotation during recrystallization *J. Appl. Phys.* **33** 2958–65

[42] Schatt W 1992 *Sintervorgänge* 1st edn (Düsseldorf: VDI)

[43] Wellner P, Gessinger G H and Exner H-E 1974 Der Einflußdes Pressens auf die Sinterkinetik kugelförmiger Kupferteilchen *Z. Metallk.* **65** 602–9

[44] Lányi P 1979 Strukturelle Aktivität und Verdichtungskinetik im Frühstadium des Schwindungsmaximums *PhD Thesis* Zentralinstitut für Festkörperphysik und Werkstofforschung, Dresden

[45] Staab T 1996 Positronenlebensdauerspektroskopieuntersuchungen zum Sinterprozeßin Metallpulverpreßlingen—Der Einflußvon Gefüge und Mikrostruktur auf den Materialtransport *PhD Thesis* Martin-Luther Universität Halle-Wittenberg

[46] Johnson D L and Clarke T M 1964 Grain boundary and volume diffusion in the sintering of silver *Acta Metall.* **12** 1173–9

[47] Ashby M F 1974 A first report on sintering diagrams *Acta Metall.* **22** 275–89